PCCP

ROYAL SOCIETY OF CHEMISTRY

PAPER

View Article Online
View Journal

Cite this: DOI: 10.1039/d6cp00755d

Influence of blend composition on morphology and exciton-charge dynamics in MEH-PPV: PMMA thin films

Jung Won Yoon, Habtom B. Gobeze and Kirk S. Schanze *

The interplay between morphology and exciton and polaron dynamics defines the photophysics of conjugated polymer blends. A systematic series of MEH-PPV:PMMA blend films, spanning from dilute dispersions to pristine MEH-PPV and ternary blends with $PC_{61}BM$, was investigated. Absorption and photoluminescence (PL) spectra confirmed conserved electronic signatures across compositions, while fluorescence lifetime imaging microscopy revealed a continuous transition from uniform dispersion to nano-aggregation and micro phase separated networks. PL lifetime histograms showed a sharp decrease in lifetime at low fractions of MEH-PPV in PMMA, followed by a plateau in lifetimes at 10–25 wt%, identifying regimes where interchain interactions dominate exciton dynamics. Incorporation of $PC_{61}BM$ to the MEH-PPV:PMMA blends gives rise to significant reduction in exciton lifetime and introduced charge-transfer signatures consistent with electron transfer. Femtosecond transient absorption spectroscopy corroborated these pathways, resolving ultrafast singlet exciton decay, and formation of long-lived polarons combined with fullerene anion-radical absorption. The dynamics of charge-transfer and polaron decay are dominated by the local concentration of $PC_{61}BM$ in the MEH-PPV phase, as the acceptor is dispersed and partitions between the MEH-PPV and PMMA domains. The results establish a composition-resolved link between blend morphology and exciton and polaron dynamics, suggesting a pathway for controlling exciton and charge pathways in conjugated polymer systems.

Received 28th February 2026,
Accepted 4th May 2026

DOI: 10.1039/d6cp00755d

rsc.li/pccp

Introduction

The performance of conjugated polymer thin films in optoelectronic devices is determined not only by chemical structure, but also by nano- and microstructural organization of the materials in the solid state. In solution-processed films, domain formation, chain packing, and polymer aggregation regulate exciton migration, charge generation, and exciton and charge recombination lifetimes.[1–5] Polymer blending represents a versatile and scalable strategy; by dispersing a conjugated polymer within an inert host, one can modulate interfacial density, percolation pathways, and local dielectric environments, all while preserving low-cost and solution-based processing.[6–15]

Poly[2-methoxy-5-(2-ethylhexyloxy)-1,4-phenylene vinylene] (MEH-PPV) has long served as a prototypical light-emitting and hole-transporting conjugated polymer.[16,17] It readily forms uniform thin films by spin coating and has been integrated into diverse device platforms.[18–22] The optical emission, exciton diffusion, and hole-transport properties of MEH-PPV are well-documented,[23,24] and numerous studies have examined its behavior in copolymers and in blends with insulating matrices such as poly(methyl methacrylate) (PMMA) and polystyrene.[18,25–29] These investigations demonstrate that processing conditions and composition strongly affect polymer packing, domain size, and interfacial area, with direct implications for emission spectra, exciton lifetime, and overall device efficiency.[30] Despite this foundation, systematic composition-resolved studies on polymer blends that directly correlate morphology, excited-state lifetimes, and charge-transfer pathways are underexplored. In particular, the progression from homogeneous dispersion to micro-aggregation and ultimately to phase separation has not yet been quantitatively mapped onto excited-state dynamics. Moreover, when electron acceptors such as $PC_{61}BM$ ([6,6]-phenyl-C_{61}-butyric acid methyl ester) are introduced, photoinduced electron transfer is expected to compete with exciton decay, but its connection to the morphology continuum has not been resolved with spatial specificity.

In previous work, we demonstrated that MEH-PPV/PMMA blends undergo composition-dependent phase segregation, forming nano- and microscale domains whose characteristic size increases with increasing MEH-PPV concentration.[18] At low MEH-PPV fractions, the conjugated polymer exists as dispersed domains within the PMMA matrix, whereas higher

Department of Chemistry, University of Texas at San Antonio, One UTSA Circle, San Antonio, Texas, 78249, USA. E-mail: kirk.schanze@utsa.edu, iyjw1118@gmail.com, Habtom.Gobeze@utsa.edu

concentrations lead to domain coarsening and the development of continuous MEH-PPV-rich regions.[18] However, the excited-state dynamics associated with this morphological evolution were not examined. Therefore, in the current study we investigate the photoluminescence properties and excited-state dynamics of spin-coated films comprising binary blends of MEH-PPV with PMMA, as well as ternary blends that include MEH-PPV, PMMA, and the electron acceptor $PC_{61}BM$. In the binary and ternary blend films, the MEH-PPV fraction in PMMA was systematically varied, with and without the incorporation of $PC_{61}BM$. Fluorescence lifetime imaging microscopy (FLIM) was employed to visualize spatial heterogeneity and quantify lifetime distributions in mixed and phase-segregated domains, while femtosecond transient absorption (TA) spectroscopy was used to resolve exciton decay, polaron formation, and charge transfer in nano- and microphase-segregated ternary blends. Together, these approaches give a composition-resolved understanding of how morphology, exciton dynamics, and charge separation vary in polymer blend films with conjugated and non-conjugated polymers.

Results and discussion

Composition-dependent optical properties of MEH-PPV:PMMA blends

To establish a baseline for composition-dependent properties, a systematic series of binary blend MEH-PPV:PMMA thin films was prepared by spin coating, with MEH-PPV fractions ranging from 1 to 100 wt% (corresponding to pristine MEH-PPV). Eight film compositions were fabricated and are summarized in the composition map in Fig. 1a. The corresponding UV–visible absorption and photoluminescence (PL) spectra of the films are shown in Fig. 1b and 1c, serving as a steady-state reference for the time-resolved analyses presented later. The absorption spectra exhibit the characteristic π, π^* transition of MEH-PPV centered around 500–520 nm, with the overall spectral profile remaining consistent across the composition range. The monotonic increase in absorbance reflects the higher chromophore density, while the consistent absorption band shape indicates that the backbone electronic structure of MEH-PPV is maintained, and that the blend composition has little effect on the absorption bandshape.

The PL spectra, by contrast, show systematic changes that reflect evolving nano- and microstructure across the blend series (Fig. 1c and Table S1). While total emission intensity increases with MEH-PPV fraction due to the increasing chromophore concentration, more meaningful insight comes from the evolution of the PL bandshape with composition. The primary emission peak (λ_{00}) red-shifts slightly from 566 nm at 1 wt% MEH-PPV in PMMA, to a maximum of 578 nm at 5 wt% MEH-PPV, before gradually blue-shifting back to 568 nm in the pristine (100%) MEH-PPV film. This trend suggests that there is a change in the local environment of the conjugated polymer

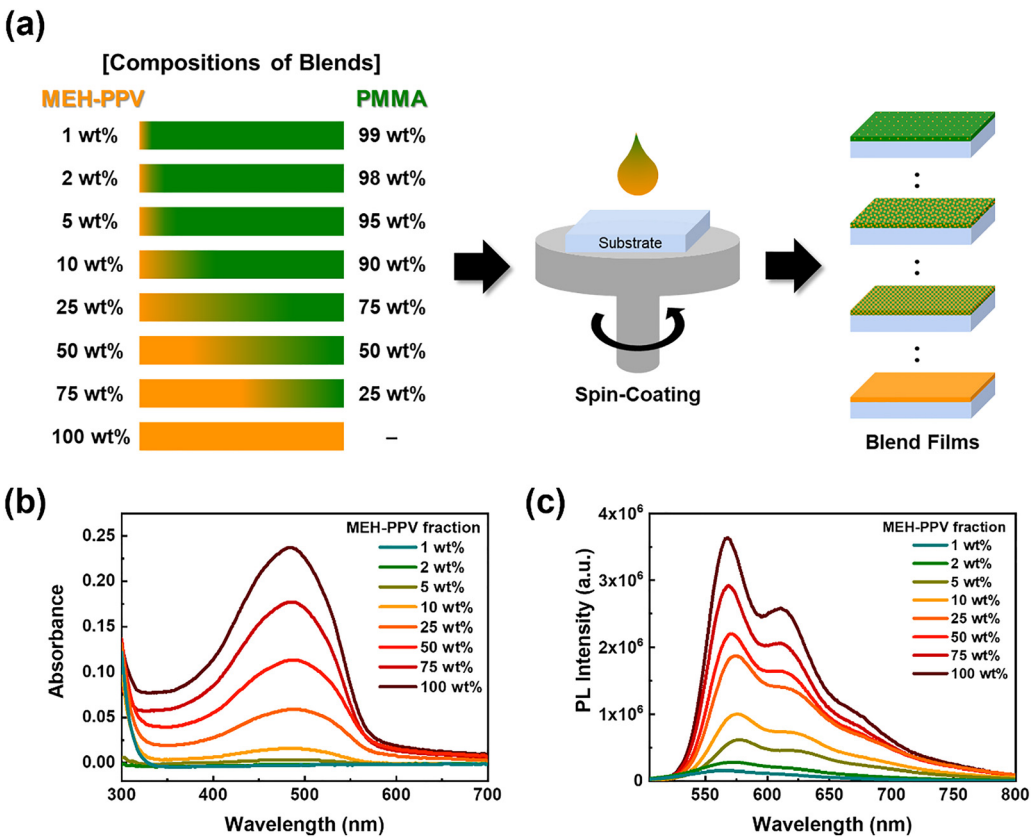

Fig. 1 (a) Polymer blend compositions used in this study (MEH-PPV fraction in PMMA; labels denote wt%, uniform films). (b) Absorption and (c) emission spectra of MEH-PPV/PMMA blend films.

chains with blend composition. These effects could include a change in effective dielectric (PMMA has an effective dielectric constant of 6–7),[31] and on intra- and interchain interactions within the MEH-PPV domains as the degree of phase separation increases along the series (see below).[32,33] Consistently, the vibronic intensity ratio (I_{00}/I_{01}) decreases overall with increasing MEH-PPV fraction, dropping from 1.75 to 1.34 across the 1–50 wt% MEH-PPV range, before slightly increasing at higher fractions (Table S1). A high I_{00}/I_{01} ratio is typically associated with emission from isolated chains,[34] whereas a reduced ratio reflects stronger interaction coupling, increased exciton delocalization, and the growing contribution of aggregate states.

These spectral characteristics suggest a three-stage morphological transition, from molecularly dispersed chains at low fractions to loosely associated nano- and micro-phase-separated domains, with aggregation and enhanced electronic coupling, and eventually to bicontinuous, phase-separated MEH-PPV domains. The minor recovery of I_{00}/I_{01} at the highest fraction may point to optical decoupling within large, phase-separated domains, where emission increasingly originates from less strongly coupled chain segments rather than fully aggregated cores. Altogether, the steady-state optical trends establish a clear signature of composition-driven microstructural blend evolution and anticipate the more detailed picture provided by FLIM and transient absorption. In these measurements, exciton lifetimes, heterogeneity, and charge-transfer dynamics can be directly correlated with composition-dependent morphology.

Fluorescence lifetime imaging of morphology and excited-state heterogeneity

Confocal FLIM was applied to image how composition-controlled microstructures give rise to variation in the PL dynamics in the binary blend MEH-PPV:PMMA films. All FLIM images were acquired with 485 nm pulsed excitation, with emission detected through 485 nm dichroic and 488 nm long-pass filters. The confocal FLIM images shown in Fig. 2a display the spatial variation of the median fluorescence lifetime as a false color map.[35] Fixed image size and lifetime-color scale were applied across all samples, enabling direct comparison of the morphology and lifetime as a function of film composition. FLIM Images with lower and higher resolution are included in the supporting information (Fig. S1 and S2, respectively). First, consistent with the previous study of MEH-PPV:PMMA blends,

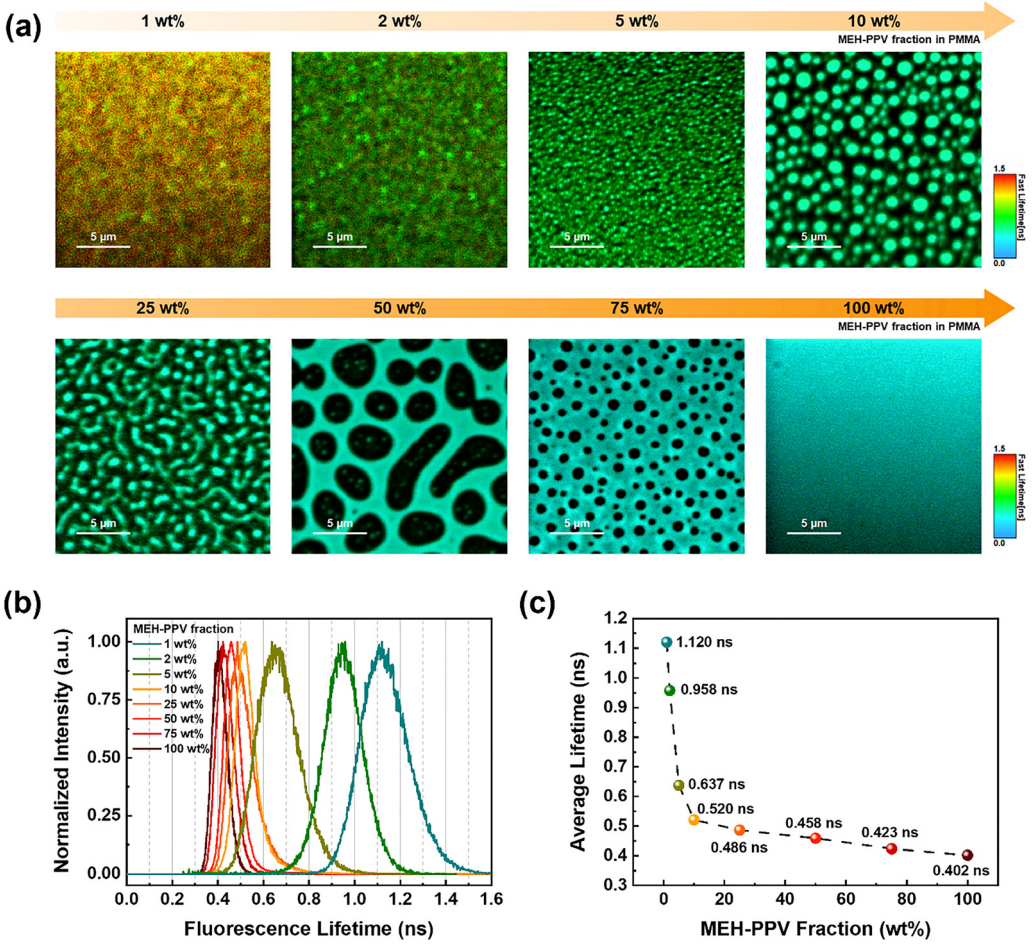

Fig. 2 (a) Fluorescence lifetime maps with color scale at right (0–1.5 ns, blue → green → red). (b) PL lifetime histogram corresponding to the FLIM images in (a). (c) Plot of median PL lifetime from the histogram of MEH-PPV:PMMA blend films as a function of binary blend composition.

which relied on wide-field fluorescence imaging,[18] we found that the film morphology exhibits increased segregation between MEH-PPV and PMMA domains with increasing MEH-PPV loading. In the very low regime at 1% MEH-PPV, the FLIM image is relatively uniform; however, on the length scale <1 μm there is evidence of clustering of the MEH-PPV regions, with distinct evidence of some aggregated MEH-PPV domains dispersed in the PMMA host (see Fig. S2a). As the loading of MEH-PPV increases to 5%, there is clear evidence of nano-phase segregation, where the MEH-PPV regions appear as distinct bluish-green clusters (<0.5 μm, Fig. S2c) surrounded by dark regions corresponding to the PMMA host domains. Above 5% MEH-PPV, the domain structure becomes distinct, with MEH-PPV domains increasing in size, and above 50% MEH-PPV, distinct phase-separated networks are apparent (see Fig. S14 for histograms of domain sizes in the blends).[18]

More interesting is the variation of the MEH-PPV PL lifetime as function of blend composition. First, inspection of the FLIM false-color images reveals an evolution in the median decay lifetime as evidenced from the yellow-red color for the 1% MEH-PPV film towards a green to green-blue coloration with increasing MEH-PPV fraction. More quantitative insight comes from the PL lifetime histograms and graph of average lifetimes that are shown in Fig. 2b and c. It is evident that at low MEH-PPV loading, the average PL lifetime is longer ($\sim$1.1 ns) and then it decreases sharply to 10% MEH-PPV ($\sim$0.52 ns) and then more gradually with increasing MEH-PPV loading. We hypothesize that the median lifetime reflects the extent of interchain interactions (aggregation) that occur within the MEH-PPV domains. At the very lowest loading, the MEH-PPV is mostly dispersed in the PMMA host, and interchain aggregation is suppressed. However, as the concentration of MEH-PPV increases, the degree of interchain interactions sharply increases and giving rise to quenching of the intrachain exciton as reflected by the sharp decrease in PL lifetime.

FLIM images of the blend films (1–10% MEH-PPV) with higher resolution are shown in Fig. S2. Close inspection of these images reveals that within a single blend composition, there is a clearly defined spatial variation of PL lifetime that suggests that the degree of MEH-PPV interchain aggregation increases with the polymer's local concentration in the blend. Most striking is the image of the 2% MEH-PPV blend (Fig. S2b), where there are distinct regions where the local concentration of MEH-PPV is higher, and these display a shorter average lifetime (blue) than the surrounding regions (green) where the MEH-PPV is more dispersed within the PMMA host. The shorter average lifetime is also apparent within the center of the nano-domains (sky blue) in the 5% blend (Fig. S2c), and these are surrounded by regions with relatively longer lifetime (green) where the MEH-PPV is more dispersed by the PMMA host. While there is some spatial variation in the MEH-PPV lifetime in the low concentration blends, at concentrations above where domain coarsening onsets (*i.e.* $\geq$5% MEH-PPV) the lifetime is comparatively uniform within the MEH-PPV domains regardless of domain size.

Taken together the FLIM results reveal how composition-dependent microstructures in MEH-PPV:PMMA binary blend films give rise to pronounced spatial and compositional variations in the excited-state dynamics of the intrachain exciton. Across the series, the fixed-scale FLIM maps in Fig. 2a demonstrate a clear evolution from nearly uniform lifetimes at very low MEH-PPV loading, where isolated MEH-PPV chains are largely dispersed within the PMMA matrix, to increasingly pronounced domain formation as the MEH-PPV fraction rises. At low loadings (1–5%), nanoscale clusters emerge, and regions of locally higher MEH-PPV concentration exhibit noticeably shorter lifetimes, signaling enhanced interchain aggregation that gives rise to exciton quenching. As the MEH-PPV content increases further, these domains grow (Fig. S14) and develop into distinct phase-separated regions, wherein the PL lifetime approaches that of pristine MEH-PPV. Complementary lifetime histograms (Fig. 2b) confirm that the average PL lifetime decreases sharply with increasing MEH-PPV fraction, consistent with stronger interchain interactions and exciton quenching within aggregated domains. Higher-resolution FLIM images further show evidence of PL lifetime heterogeneity within each blend, showing that even within a single composition, local variations in MEH-PPV concentration produce measurable variation in the PL lifetime.

Morphology of ternary blends featuring MEH-PPV, $PC_{61}BM$ and PMMA

We also set out to probe the dynamics of charge separation and recombination in ternary blends that feature MEH-PPV and electron acceptor $PC_{61}BM$ dispersed into a PMMA host matrix. The goal of this line of work was to explore whether the efficiency and dynamics of photoinduced electron transfer from MEH-PPV to $PC_{61}BM$ depend on blend composition, phase segregation and domain size. Two ternary blend compositions were investigated. In both cases, the weight ratio of MEH-PPV to $PC_{61}BM$ was fixed at 2 : 1, while the total loading of the 2 : 1 MEH-PPV/$PC_{61}BM$ mixture in PMMA was varied. The compositions were: Ternary-10 (10 : 5 : 85 wt% MEH-PPV/$PC_{61}BM$:PMMA) and Ternary-25 (25 : 12 : 63 wt% MEH-PPV/$PC_{61}BM$:PMMA).

The first step of this work was to explore how the morphology of the ternary blends is modified by the addition of $PC_{61}BM$. The ternary blend films were cast onto glass substrates, and imaged with FLIM, atomic force microscopy (AFM), and Kelvin probe force microscopy (KPFM). The images of the two ternary blend compositions are summarized in Fig. 3.

First, inspection of the FLIM images for the Ternary-10 and Ternary-25 blends (Fig. 3a and d) shows that, like in the binary blends, there still is a distinct segregation between the MEH-PPV and PMMA domains. In particular, the FLIM images of the ternary blends reveal circular domains of fluorescent material (MEH-PPV) surrounded by the (dark) PMMA host. Ternary-10 shows MEH-PPV domain sizes 0.5–1 μm, with some smaller regions, whereas in Ternary-25 the domain sizes increase to the range 0.5–3 μm with more size dispersity (see domain size histograms in Fig. S15). The FLIM images and PL lifetime histograms (Fig. S5) show that the lifetime is considerably

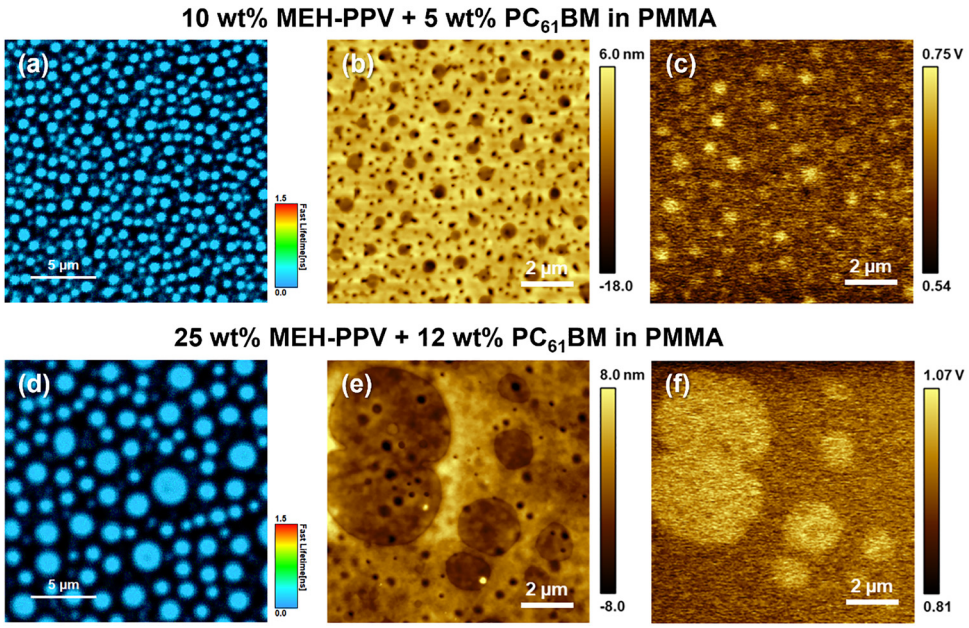

Fig. 3 (a)–(c) FLIM, AFM height images, and KPFM surface potential of Ternary-10 (MEH-PPV/$PC_{61}BM$:PMMA, 10 : 5:85 wt%). (d)–(f) FLIM, AFM height images, and KPFM surface potential of Ternary-25 (MEH-PPV/$PC_{61}BM$:PMMA, 25 : 12 : 63 wt%).

reduced in both ternary blends compared to the binary blends, with a peak median PL lifetime of ~165 ps and ~120 ps for the Ternary-10 and -25 blends, respectively. The decreased lifetimes are due to quenching of the MEH-PPV exciton by charge transfer to $PC_{61}BM$.[31]

AFM and KPFM images of the ternary blends provide further insight into the morphology of the films. For Ternary-10, the AFM image (Fig. 3b) shows that the MEH-PPV regions appear as "valleys" with relatively lower height compared to the surrounding PMMA host. The corresponding KPFM image (Fig. 3c) shows good contrast between the MEH-PPV and PMMA domains, with higher surface potential (lower work function) corresponding to the MEH-PPV domains. The morphology of the Ternary-25 blends is more complex, with the AFM image (Fig. 3e) showing the circular MEH-PPV domains as depressed circular regions that are surrounded by the PMMA host. As for the Ternary-10 blends, the KPFM image of the Ternary-25 blends shows that the surface potential of the circular (MEH-PPV) regions is higher than the surrounding domains.

It is not clear whether the $PC_{61}BM$ preferentially segregates into the MEH-PPV or PMMA domains; however, we can make some predictions as follows. First, the solubility parameter of $PC_{61}BM$ (9.37 $(cal\ cm^{-3})^{1/2})$[36] is more closely matched to PMMA (9.2 $(cal\ cm^{-3})^{1/2})$[37] than to MEH-PPV (10.06 $(cal\ cm^{-3})^{1/2})$.[38] This suggests that we should not expect that $PC_{61}BM$ will selectively partition into the MEH-PPV domains; rather it is likely distributed between both polymer domains within the ternary blend films. Nevertheless, it is quite evident from the quenching of the MEH-PPV PL lifetime in the ternary blends (*e.g.*, Fig. S5) that there must be a considerable fraction of the $PC_{61}BM$ electron acceptor present in the MEH-PPV domains in both the Ternary-10 and -25 blend films.

Femtosecond transient absorption of binary and ternary blends. Effects of blend morphology on exciton dynamics and charge transfer

Femtosecond transient absorption (TA) spectroscopy was applied to provide insight into the exciton dynamics and charge transfer in the binary MEH-PPV:PMMA blends, and the ternary blends that contained $PC_{61}BM$ electron acceptor. Initial studies compared the spectroscopy and dynamics of 10% and 25% MEH-PPV:PMMA binary blends with those of a pristine MEH-PPV film (Fig. 4).

As shown in Fig. 4a, the TA spectra of MEH-PPV are characterized by strong negative band extending from 450–600 nm that corresponds to the ground state absorption bleach (GSB) and stimulated emission (SE), along with a broad near-infrared (near-IR) band extending from 900–1600 nm with several weaker, and narrower features in the 800–900 nm range. Previous studies have examined MEH-PPV transient absorption, and the broad near-IR feature is attributed to the singlet exciton (E), and the shorter wavelength absorption bands are attributed to the polaron (P, charged) states produced by exciton splitting.[39] The GSB samples both the exciton and polaron states.

Of interest is the comparison of the femtosecond TA spectra and dynamics of the binary blends with the pristine MEH-PPV. The time resolved spectra for the 25% MEH-PPV:PMMA binary blend is shown in the bottom panel of Fig. 4a, while the spectra for the 10% binary blend are shown in Fig. S8. The TA dynamics at the ground state bleach (529 nm) and the exciton absorption band (1215 nm) are overlaid for the three samples in Fig. 4b and c. Generally, the TA spectra and dynamics are very similar for the pristine and binary blend films, with the prominent

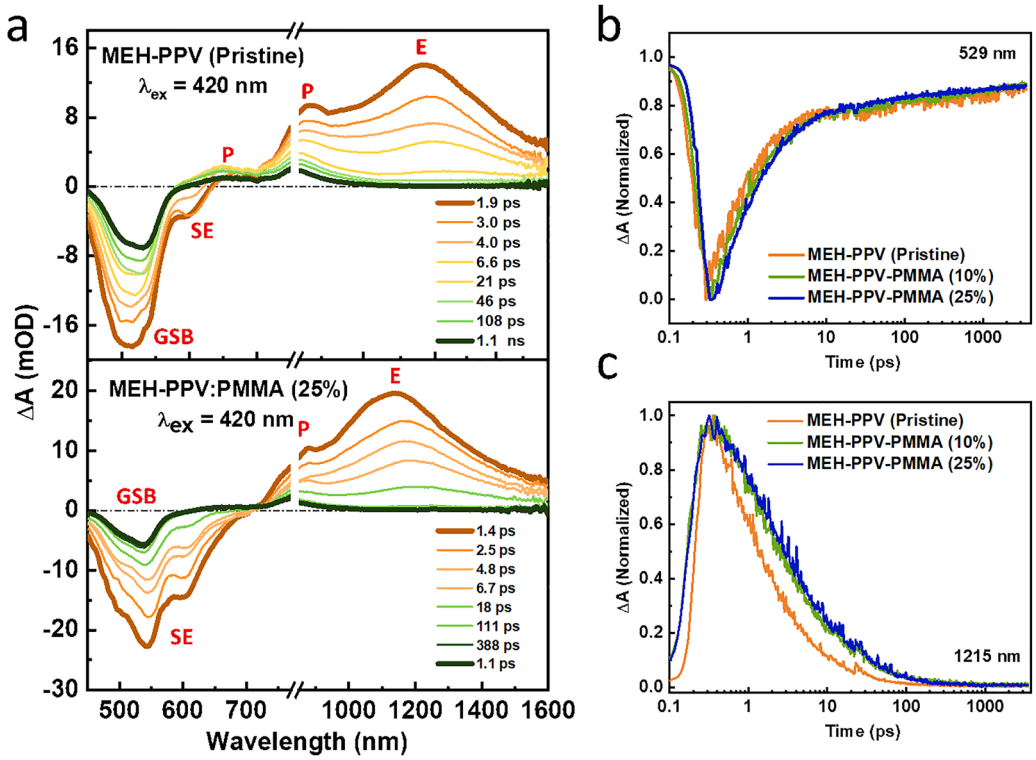

Fig. 4 (a) Visible-near-IR femtosecond TA spectra of (top) pristine film of MEH-PPV and (bottom) 25% MEH-PPV:PMMA binary blend film. Time delays provided in the legend. (b) and (c) Overlay of normalized TA dynamics for pristine MEH-PPV, 10% MEH-PPV:PMMA and 25% MEH-PPV:PMMA binary blend films at 529 nm (c) and 1215 nm (d). All experiments conducted with 420 nm excitation, 100 nJ pulse^{-1}.

exciton band (E) in the near-IR and ground state bleach and ground state bleach and stimulated emission (GSB, SE) in the visible. However, close inspection does reveal some differences. Specifically, in both binary blend films, the stimulated emission is relatively stronger compared to the ground state bleach. Moreover, at long delay times the spectrum of the pristine MEH-PPV film shows more evidence for the polaron (P) absorption features. Another clear difference is that the two binary blend films show noticeably slower decay dynamics in the exciton band (Fig. 4c, 1215 nm). This is clearly manifested in the fits of the 1215 nm exciton dynamics shown in Fig. 13b, where we see that each of the lifetime components increases in the sequence MEH-PPV < 25% MEH-PPV < 10% MEH-PPV. These differences are consistent with the observations from the PL lifetime measurements, which show that the lifetime is on average longer in the 10% and 25% binary blends compared to the pristine MEH-PPV film. Taken together, the femtosecond TA study of the binary blends suggests that the degree of MEH-PPV aggregation that gives rise to exciton quenching and splitting into polaron states is suppressed compared to the pristine film.

Addition of $PC_{61}BM$ to the MEH-PPV:PMMA blend films leads to significant changes in the femtosecond TA spectra and dynamics, consistent with photoinduced charge transfer from the polymer to the fullerene acceptor. Insight concerning the effect of the blend composition on the process comes from comparison of the spectra and dynamics in the ternary blends, and comparison to films which contain 2 : 1 MEH-PPV:$PC_{61}BM$ (wt : wt), and pristine MEH-PPV. Fig. 5a compares the time resolved spectra for 2 : 1 MEH-PPV:$PC_{61}BM$ and Ternary-25, which contains MEH-PPV, $PC_{61}BM$ and PMMA. For the 2 : 1 blend, it is seen that even at 1 ps time delay, the near-IR exciton band is quenched, and the spectrum is dominated by the polaron bands (P) and the GSB. By contrast, at early times the Ternary-25 blend spectrum shows some residual exciton band in the near-IR, along with the bands associated with the polaron states produced by charge transfer. We also note that there is a small, but clear weak peak in the near-IR at ~1050 nm that can be assigned to the reduced $PC_{61}BM$.[40,41] By comparison, the time resolved spectra of the Ternary-10 film (Fig. S12) exhibit a more pronounced exciton band in the near-IR, and stimulated emission in the visible, indicating that MEH-PPV to $PC_{61}BM$ charge transfer is slower and less efficient. Nevertheless, there is still some evidence for charge transfer to $PC_{61}BM$ by the existence of the polaron bands and the weak 1050 nm peak due to the reduced fullerene.

Further insight into the dynamics and efficiency of MEH-PPV → $PC_{61}BM$ charge transfer can be obtained by comparing the transient absorption (TA) dynamics at the wavelengths associated with the ground-state bleach (GSB, 529 nm) and the exciton absorption (1215 nm) shown in Fig. 5b and c, respectively. The decay of the exciton absorption (Fig. 5c) directly reflects the timescale of charge transfer from MEH-PPV to $PC_{61}BM$. Here, the exciton decay rate follows the

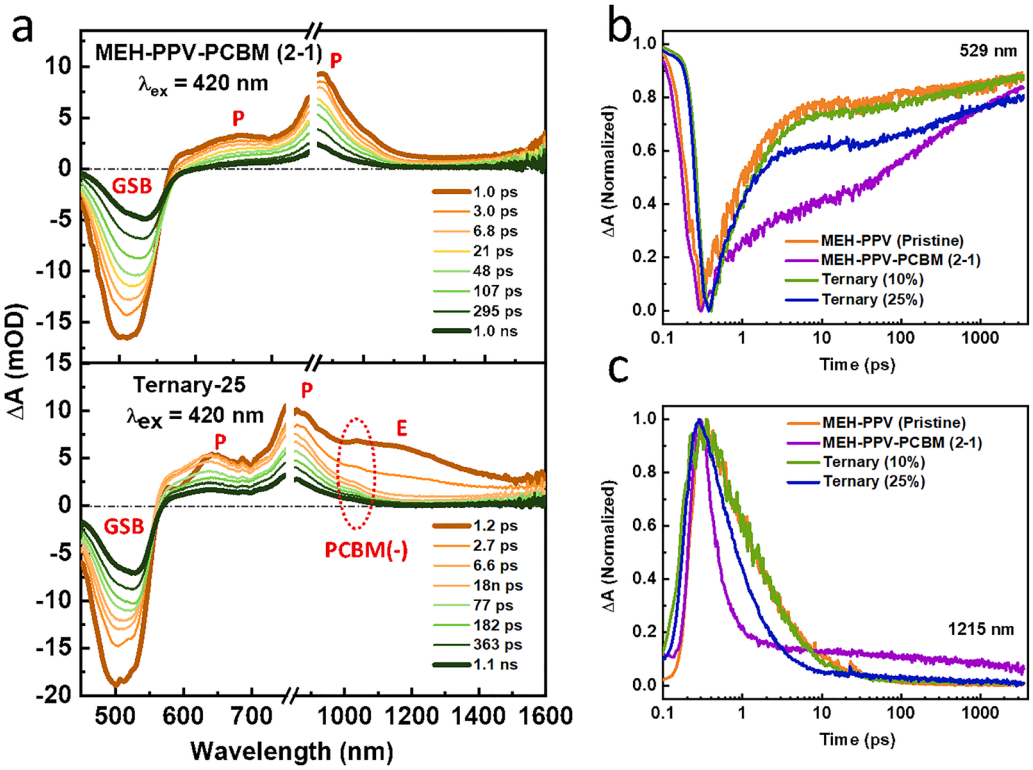

Fig. 5 (a) Visible-near-IR femtosecond TA spectra of (top) 2 : 1 MEH-PPV/$PC_{61}BM$ and (bottom) Ternary-25 blend film. Time delays provided in the legend. (b) and (c) Overlay of normalized TA dynamics for pristine MEH-PPV, 2 : 1 MEH-PPV/$PC_{61}BM$, Ternary-10 and Ternary 25 blend films at 529 nm (c) and 1215 nm (c). All experiments conducted with 420 nm excitation, 100 nJ $pulse^{-1}$.

sequence 2 : 1 MEH-PPV:$PC_{61}BM$ > Ternary-25 > Ternary-10 ≈ pristine MEH-PPV, indicating a corresponding decrease in photoinduced charge-transfer efficiency. The GSB dynamics at 529 nm (Fig. 5b) reinforce this interpretation. The GSB amplitude at intermediate delay times (10–100 ps) reflects the charge-transfer efficiency, and it follows the same trend: 2 : 1 MEH-PPV:$PC_{61}BM$ > Ternary-25 > Ternary-10 > pristine MEH-PPV. These observations demonstrate that both exciton decay and GSB amplitude consistently track the relative efficiencies of charge transfer across the sample series. Taken together, the femtosecond TA results show that the rate of MEH-PPV → $PC_{61}BM$ charge transfer and the overall efficiency of charge separation are different in the Ternary-25 and -10 blends compared to the 2 : 1 MEH-PPV:$PC_{61}BM$ mixture.

General discussion

This study explored the relationship between polymer blend composition and photophysics in binary blends that contain MEH-PPV as a photoactive, semiconducting polymer and PMMA as a photoinactive, insulating matrix. The work also explored charge separation in ternary blends which contain the electron acceptor $PC_{61}BM$, in addition to MEH-PPV and PMMA. The work is fundamental in nature, yet it has implications for optoelectronic applications of conjugated polymers.[42–45] Of primary interest in this work is how mixing the inert PMMA with the MEH-PPV affects the photophysical properties of the blends.

Previous studies have extensively explored the effects of polymer aggregation on the photophysics of conjugated polymers, including MEH-PPV as well as other polymers such as poly(3-hexylthiophene).[1–3,23,24,26,46,47] In general, it is observed that when the conjugated polymers are in solution in a molecularly dissolved, unaggregated state, the exciton lifetime and PL efficiency are enhanced. As the chains aggregate, the exciton lifetime and PL efficiency are reduced due to interchain interactions, presumably due to formation of interchain excimer or charge transfer states (polaron states).[1,2,23,24] Studies of single chains of MEH-PPV dispersed in PMMA suggest that the chain conformation can also influence the exciton emission efficiency by affecting intrachain exciton–exciton annihilation.[48]

Across the MEH-PPV:PMMA binary blend series, the steady state PL spectra and FLIM track a morphological progression from isolated MEH-PPV chains to nano aggregates and finally to phase separated, percolated MEH-PPV domains. FLIM images acquired under identical excitation/detection conditions reveal that the median PL lifetime drops rapidly as MEH-PPV fraction increases from ~1.1 ns in the most dilute films to ~0.52 ns by 10 wt%, followed by a more gradual decline thereafter. The corresponding lifetime histograms and fixed scale maps show that the PL lifetime distribution narrows and shifts to shorter lifetime consistent with increased interchain interactions (aggregation) as the MEH-PPV fraction increases. Importantly, sub-micrometer FLIM maps at intermediate compositions (*e.g.*, 2–5 wt%) reveal distinct lifetime

heterogeneity within the blend films. This spatially resolved behavior indicates that local polymer concentration governs exciton quenching pathways *via* interchain interactions in MEH-PPV. Femtosecond TA study of the binary blends provides further support for the conclusion that interchain aggregation of the MEH-PPV is suppressed in the blends. In particular, the near IR interchain exciton band (~1215 nm) decays more slowly in the binary blends than in pristine MEH-PPV, and the late time spectra show comparatively weaker polaron absorptions. These observations imply that dilution in PMMA suppresses the interchain configurations that favor ultrafast exciton splitting into polarons.

Previous studies using single molecule techniques reported that the "single photon" emission efficiency of single MEH-PPV chains in PMMA varies with molecular weight, which is the result of intrachain exciton migration which is enhanced when the chains are collapsed in the PMMA host.[48] The present work was carried out with a single molecular weight sample of MEH-PPV (~205 000 g mol^{-1}) and at relatively high concentrations in the PMMA host, and therefore it is not possible to draw any conclusions regarding the effect of intrachain exciton migration on the present results. It is also likely that the molecular weight of the MEH-PPV will influence the concentration dependence of phase segregation that is observed in the current study further complicating the relationship between molecular weight and intrachain *vs.* interchain effects.

Introducing $PC_{61}BM$ into the PMMA host with fixed MEH-PPV:$PC_{61}BM$ ratio (2 : 1, wt : wt) preserves the overall phase segregated domain topology. The MEH-PPV is present as circular fluorescent regions within the PMMA matrix; however, the sharply reduced PL lifetimes are consistent with exciton quenching by charge transfer. The solubility parameter analysis suggests that $PC_{61}BM$ does not segregate exclusively into MEH-PPV; rather, it is likely distributed between both MEH-PPV and the PMMA domains. Nevertheless, the pronounced lifetime quenching demands that a significant fraction of $PC_{61}BM$ resides within or in close proximity to MEH-PPV rich regions where excitons are generated. In the presence of $PC_{61}BM$, femtosecond TA shows that the near-IR exciton band is strongly quenched, and the TA spectra display polaron bands along with a weak feature near 1050 nm assigned to the $PC_{61}BM$ anion. The relative charge transfer (CT) efficiencies scale as 2 : 1 MEH-PPV:$PC_{61}BM$ > Ternary-25 > Ternary-10. This trend likely signals that even though the ratio of MEH-PPV:$PC_{61}BM$ is the same in the ternary blends, the local concentration of $PC_{61}BM$ in the MEH-PPV domains is higher in Ternary-25 than in Ternary-10. Taken together, the TA results show that the charge transfer kinetics and yields are governed by how the blend composition dictates local MEH-PPV and $PC_{61}BM$ concentration and domain morphology.

A key distinction between the binary MEH-PPV:PMMA blends and the ternary MEH-PPV:$PC_{61}BM$:PMMA blends is the introduction of an additional, competing excited-state decay pathway in the latter. In the binary blends, dilution of MEH-PPV in PMMA primarily modulates exciton dynamics by controlling interchain interactions and aggregation, leading to composition-dependent variations in exciton lifetime without introducing new electronic states. By contrast, incorporation of $PC_{61}BM$ in the ternary blends introduces an efficient electron transfer pathway that competes directly with intrinsic exciton decay. As a result, while exciton lifetimes in the binary blends reflect aggregation controlled quenching within MEH-PPV domains, the markedly shorter lifetimes observed in the ternary blends arise predominantly from charge transfer to $PC_{61}BM$. Importantly, although the MEH-PPV:$PC_{61}BM$ ratio is fixed at 2 : 1 in the ternary films, the charge transfer efficiency varies strongly with the ternary blend composition. This indicates that local acceptor concentration within MEH-PPV-rich domains is controlled by the overall ternary composition rather than just by the MEH-PPV:$PC_{61}BM$ stoichiometry. Thus, the transition from a binary to a ternary blend fundamentally changes the role of morphology from governing exciton quenching pathways in the binary system to additionally regulating charge separation pathways in the ternary system.

Conclusion

This work provides a composition resolved study of how blend morphology governs exciton and charge dynamics in based polymer blend films consisting of MEH-PPV and PMMA. Across the binary blend series, steady state spectroscopy, FLIM imaging, and femtosecond transient absorption together show a clear progression from isolated chains to nanoscale aggregates and finally to phase separated MEH-PPV domains. This evolution is accompanied by strong, composition dependent modulation of the exciton lifetime: dilute blends suppress interchain interactions and exhibit long lifetimes, whereas increased MEH-PPV loading enhances aggregation, leading to fast exciton quenching. Spatially resolved FLIM maps further show that even within a single blend composition, local variations in polymer concentration yield measurable variations in PL lifetime, highlighting the important role of nanoscale heterogeneity in determining excited state behavior.

Introduction of $PC_{61}BM$ into the MEH-PPV:PMMA blends introduces photoinduced electron transfer as an additional exciton decay pathway that competes with intrinsic exciton decay. Both FLIM and transient absorption confirm that exciton lifetimes are strongly reduced in the ternary blend films and that charge transfer efficiency depends strongly on blend composition. The ranking of charge transfer efficiency (2 : 1 MEH-PPV:$PC_{61}BM$ > Ternary-25 > Ternary-10) indicates that local acceptor concentration and domain morphology determine the rate and yield of charge separation. Observation of fullerene anion signatures and long lived polarons further verifies the formation of charge separated states in the ternary blends. However, notable is that the lifetime of the charge separated states is not strongly influenced by the blend composition. Whereas binary MEH-PPV:PMMA blends demonstrate how morphology modulates exciton lifetime through aggregation effects, the ternary blends reveal how the same morphological variation governs the efficiency and kinetics of

photoinduced charge transfer by controlling the local distribution of the electron acceptor.

Taken together, the results presented here provide a unified picture that correlates blend composition, morphology, and excited state dynamics in systems consisting of a blend of a conjugated polymer and an inert, non-conjugated polymer. By demonstrating how nanoscale blend domain structure controls both exciton quenching and interfacial electron transfer, this study offers guiding principles for designing polymer blends that balance exciton harvesting, charge generation, and transport. Such insights are broadly relevant to the optimization of emissive, photovoltaic, and charge transporting polymers, where compositional tuning and nanoscale morphology remain are important for controlling the material's performance.

Experimental section

Materials

Poly[2-methoxy-5-(2-ethylhexyloxy)-1,4-phenylene vinylene] (MEH-PPV, M_w = 204 800) was purchased from Ossila. Other chemicals, including poly(methyl methacrylate) (PMMA, M_w = 350 000), [6,6]-phenyl C_{61} butyric acid methyl ester ($PC_{61}BM$), 1,2-dichloroethane, and chlorobenzene, were obtained from commercial suppliers (Sigma-Aldrich) and used without further purification.

Sample preparation

Borosilicate glass substrates were used for optical, FLIM, and femtosecond TA measurements, whereas ITO-coated glass substrates were used for AFM and KPFM measurements. Substrates were cleaned by sequential ultrasonication for 10 min each in a sodium dodecyl sulfate (SDS) solution, deionized water, acetone, and isopropanol, followed by drying and plasma treatment for 15 min. Blend solutions were prepared at a total concentration of 5.2 mg mL^{-1} dissolved in 1,2-dichloroethane, with MEH-PPV fractions varied from 1 to 100 wt% to obtain the desired compositions. Ternary blends were prepared by adding $PC_{61}BM$ at half the MEH-PPV fraction (5 and 12 wt% for the 10 and 25 wt% blends, respectively) using chlorobenzene as a solvent. Films were deposited by spin-coating at 1000 rpm for 40 s.

Characterization

UV–visible absorption spectra were recorded using a Shimadzu UV-2600 spectrometer. Photoluminescence (PL) spectra were obtained with an FLS 1000 fluorescence spectrometer (Edinburgh Instruments). Time-resolved fluorescence lifetime imaging was carried with a Picoquant MicroTime 200 system equipped with hybrid PMT and avalanche photodiode detectors. Excitation was performed using a 485 nm pulsed diode laser as the excitation source (Picoquant). Emission light was detected after passing through a 488 nm long-pass filter and a ZT405/485-UF3 dichroic filter (Chroma Technology). All images were acquired under identical excitation and detection settings. Data acquisition and analysis was carried out with the SymPhoTime 64 software package (Picoquant). Each pixel of a fluorescence lifetime image represents the fast fluorescence lifetime value at the pixel. The fast lifetime corresponds to the intensity-weighted mean photon arrival time (first moment of the TCSPC decay), a fit-free lifetime metric commonly employed for rapid fluorescence lifetime imaging.[35]

Kelvin probe force microscopy (KPFM) and topographic images were acquired using a commercial atomic force microscope (NX10, Park Systems) operated in electric force microscopy (EFM)-based KPFM mode under ambient conditions. Conductive cantilevers (ElectriMulti75G, Park Systems) with a resonance frequency of ~66 kHz were used. All images were recorded over a $10 \times 10\ \mu m^2$ scan area. Surface potential images were obtained with a sample bias of 0.4 V and zero tip bias. No additional flattening or plane fitting was applied to the potential data.

Femtosecond transient absorption measurements were carried out using a HELIOS broadband pump–probe spectrometer (Ultrafast Systems) capable of detecting signals from 350 to 1600 nm in both the UV-visible and near-IR regions. The excitation pulses were provided by an amplified Ti:sapphire laser system (Astrella, Coherent, Inc.), which delivers 800 nm pulses of approximately 100 fs duration at a 1 kHz repetition rate. These pulses were directed into an OPerA Solo optical parametric amplifier (Coherent) to generate the pump wavelengths. To produce the probe continuum, a small fraction of the 800 nm output was routed through a motorized delay line and focused onto either a sapphire plate or a proprietary nonlinear crystal, yielding a white-light continuum in the visible and near-infrared ranges. Spin coated films on borosilicate glass substrates were mounted perpendicular to the incident beams and the position was rastered during data collection to minimize photodegradation. All transient absorption spectra were acquired with the samples exposed to air. Data was processed, including chirp correction and decay lifetime analysis, using the Surface Xplorer PRO software supplied by Ultrafast Systems.

Conflicts of interest

The authors declare no competing financial interest.

Data availability

The data supporting this article have been included as part of the supplementary information (SI). Supplementary information: FLIM images of polymer blends at different scales; FLIM, AFM and KPFM images of binary blends; complete set of transient absorption spectra and dynamics at selected wavelengths; parameters obtained from fits of TA kinetics (9 pages,.pdf format). See DOI: https://doi.org/10.1039/d6cp00755d.

Acknowledgements

This work was supported by the Welch Foundation through the Welch Chair at the University of Texas at San Antonio (Award No. AX-0045-20110629).

References

1 L. J. Rothberg, M. Yan, F. Papadimitrakopoulos, M. E. Galvin, E. W. Kwock and T. M. Miller, *Synth. Met.*, 1996, **80**, 41–58.
2 T.-Q. Nguyen, R. Y. Yee and B. J. Schwartz, *J. Photochem. Photobiol., A*, 2001, **144**, 21–30.
3 C. J. Collison, V. Treemaneekarn, W. J. Oldham, J. H. Hsu and L. J. Rothberg, *Synth. Met.*, 2001, **119**, 515–518.
4 M. Chang, G. T. Lim, B. Park and E. Reichmanis, *Polymers*, 2017, **9**, 212.
5 G. Qu, X. Zhao, G. M. Newbloom, F. Zhang, E. Mohammadi, J. W. Strzalka, L. D. Pozzo, J. Mei and Y. Diao, *ACS Appl. Mater. Interfaces*, 2017, **9**, 27863–27874.
6 J. Smith, R. Hamilton, I. McCulloch, N. Stingelin-Stutzmann, M. Heeney, D. D. C. Bradley and T. D. Anthopoulos, *J. Mater. Chem.*, 2010, **20**, 2562–2574.
7 G. Lu, J. Blakesley, S. Himmelberger, P. Pingel, J. Frisch, I. Lieberwirth, I. Salzmann, M. Oehzelt, R. Di Pietro, A. Salleo, N. Koch and D. Neher, *Nat. Commun.*, 2013, **4**, 1588.
8 M. Chang, Z. Su and E. Egap, *Macromolecules*, 2016, **49**, 9449–9456.
9 K. Yu, B. Park, G. Kim, C.-H. Kim, S. Park, J. Kim, S. Jung, S. Jeong, S. Kwon, H. Kang, J. Kim, M.-H. Yoon and K. Lee, *Proc. Natl. Acad. Sci. U.S.A.*, 2016, **113**, 14261–14266.
10 S. Han, X. Zhuang, W. Shi, X. Yang, L. Li and J. Yu, *Sens. Actuators, B*, 2016, **225**, 10–15.
11 T. Li, L. Xu, X. Xiao, F. Chen, L. Cao, W. Wu, W. Tong and F. Zhang, *ACS Appl. Mater. Interfaces*, 2020, **12**, 2708–2716.
12 B. Park, H. Kang, Y. H. Ha, J. Kim, J.-H. Lee, K. Yu, S. Kwon, S.-Y. Jang, S. Kim, S. Jeong, S. Hong, S. Byun, S.-K. Kwon, Y.-H. Kim and K. Lee, *Adv. Sci.*, 2021, **8**, 2100332.
13 Y. Ding, Y. Zhu, H. Wang, Y. Wang, X. Gu, X. Wang and L. Qiu, *Macromolecules*, 2022, **55**, 8577–8589.
14 L. Tang, B. Watts, L. Thomsen and C. R. McNeill, *Macromolecules*, 2021, **54**, 11134–11146.
15 Z. Zhang, Y. Wang, W. Xue, Y. Tang, C. Zhang, Y. Huang, H. Yan, S.-W. Tsang, T. Wu and S. K. So, *J. Mater. Chem. A*, 2025, **13**, 9282–9291.
16 N. S. Sariciftci, D. Braun, C. Zhang, V. I. Srdanov, A. J. Heeger, G. Stucky and F. Wudl, *App. Phys. Lett.*, 1993, **62**, 585–587.
17 G. Gustafsson, Y. Cao, G. M. Treacy, F. Klavetter, N. Colaneri and A. J. Heeger, *Nature*, 1992, **357**, 477–479.
18 N. A. Iyengar, B. Harrison, R. S. Duran, K. S. Schanze and J. R. Reynolds, *Macromolecules*, 2003, **36**, 8978–8985.
19 E. C. Chang, C. I. Chao and R. H. Lee, *J. App. Poly. Sci.*, 2006, **101**, 1919–1924.
20 H.-W. Chen, T.-Y. Huang, T.-H. Chang, Y. Sanehira, C.-W. Kung, C.-W. Chu, M. Ikegami, T. Miyasaka and K.-C. Ho, *Sci. Rep.*, 2016, **6**, 34319.
21 N. K. Abbas, I. M. Ibrahim and M. A. Saleh, *Silicon*, 2018, **10**, 1345–1350.
22 N. Sharma, C. M. S. Negi, A. S. Verma and S. K. Gupta, *J. Electron. Mater.*, 2018, **47**, 7023–7033.
23 T.-Q. Nguyen, V. Doan and B. J. Schwartz, *J. Chem. Phys.*, 1999, **110**, 4068–4078.
24 T.-Q. Nguyen, I. B. Martini, J. Liu and B. J. Schwartz, *J. Phys. Chem. B*, 2000, **104**, 237–255.
25 F. A. Feist, G. Tommaseo and T. Basché, *J. Phys. Chem. C*, 2009, **113**, 11484–11490.
26 J. Vogelsang, J. Brazard, T. Adachi, J. C. Bolinger and P. F. Barbara, *Angew. Chem., Int. Ed.*, 2011, **50**, 2257–2261.
27 C.-Y. Su and C.-C. Hua, *J. Polym. Res.*, 2017, **24**, 12.
28 S. A. Kumar, S. Gouthaman, J. S. Shankar, B. K. Periyasamy and S. K. Nayak, *Chem. Phys. Lett.*, 2021, **770**, 138462.
29 S. Hu, Y. Liao, Y. Zhang, X. Yan, Z. Zhao, W. Chen, X. Zhang, H. Liu, H. Li and L. Li, *Polymers*, 2020, **12**, 1771.
30 A. Khasbaatar, Z. Xu, J.-H. Lee, G. Campillo-Alvarado, C. Hwang, B. N. Onusaitis and Y. Diao, *Chem. Rev.*, 2023, **123**, 8395–8487.
31 A. Yadigarli, Q. Song, S. I. Druzhinin and H. Schönherr, *Beilstein J. Org. Chem.*, 2019, **15**, 2552–2562.
32 O. P. Dimitriev, D. A. Blank, C. Ganser and C. Teichert, *J. Phys. Chem. C*, 2018, **122**, 17096–17109.
33 H. Yamagata, N. J. Hestand, F. C. Spano, A. Köhler, C. Scharsich, S. T. Hoffmann and H. Bässler, *J. Chem. Phys.*, 2013, **139**, 114903.
34 F. C. Spano and H. Yamagata, *J. Phys. Chem. B*, 2011, **115**, 5133–5143.
35 T. Mandal, A. Roux and J. M. García-Arcos, in *Methods in Enzymology*, ed. J. M. Baskin, Academic Press, 2026, vol. 727, pp. 179–232.
36 N. S. Sariciftci, L. Smilowitz, A. J. Heeger and F. Wudl, *Science*, 1992, **258**, 1474–1476.
37 *Polymer Handbook*, ed. M. Huglin, J. Brandrup and E. Immergut, Wiley-Interscience, New York, 1989.
38 D. T. Duong, B. Walker, J. Lin, C. Kim, J. Love, B. Purushothaman, J. E. Anthony and T. Q. Nguyen, *J. Polym. Sci., Part B: Polym. Phys.*, 2012, **50**, 1405–1413.
39 C. Sheng and Z. V. Vardeny, in *Progress in High-Efficient Solution Process Organic Photovoltaic Devices*, ed. Y. Yang and G. Li, Springer, Heidelberg, 2015, vol. 130, Ch. 2, pp. 3–38.
40 J. W. Arbogast, C. S. Foote and M. Kao, *J. Am. Chem. Soc.*, 1992, **114**, 2277–2279.
41 F. Guo, Y.-G. Kim, J. R. Reynolds and K. S. Schanze, *Chem. Commun.*, 2006, 1887–1889.
42 N. Ananthakrishnan, G. Padmanaban, S. Ramakrishnan and J. R. Reynolds, *Macromolecules*, 2005, **38**, 7660–7669.
43 K. Kanemoto, Y. Imanaka, I. Akai, M. Sugisaki, H. Hashimoto and T. Karasawa, *J. Phys. Chem. B*, 2007, **111**, 12389–12394.
44 A. C. Grimsdale, K. Leok Chan, R. E. Martin, P. G. Jokisz and A. B. Holmes, *Chem. Rev.*, 2009, **109**, 897–1091.
45 S. Ashok Kumar, S. Gouthaman, B. K. Periyasamy and S. Lakshmi, *ACS Omega*, 2025, **10**, 30013–30022.
46 J. Guo, H. Ohkita, H. Benten and S. Ito, *J. Am. Chem. Soc.*, 2010, **132**, 6154–6164.
47 S. Lee, M. Lee, J. An, H. Ahme and C. Im, *Mol. Cryst. Liq. Cryst.*, 2013, **578**, 68–72.
48 S. Masuo, T. Tanaka, S. Machida and A. Itaya, *App. Phys. Lett.*, 2008, **92**, 233114.

